Researcher Information

Funding Information

Funding: National Basic Research Program of China (973 Program) ; **Funder Identifier:** 10.13039/501100012166 ; **Award Number:** 2017YFA0104302

Funding: Innovative Research Group Project of the National Natural Science Foundation of China ; **Funder Identifier:** 10.13039/100014718 ; **Award Number:** 61821002

Funding: Natural Science Foundation of Jiangsu Province ; **Funder Identifier:** 10.13039/501100004608 ; **Award Number:** BK20190938

Funding: National Natural Science Foundation of China ; **Funder Identifier:** 10.13039/501100001809 ; **Award Number:** 51832001

Table of contents entry

Moderate cooling coprecipitation for monodisperse extremely small iron oxide as a pH dependent T_1-MRI contrast agent.

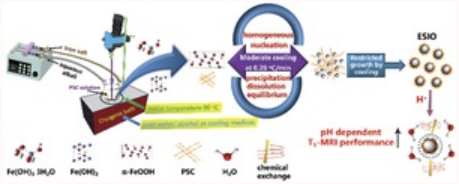

Moderate cooling coprecipitation for extremely small iron oxide as a pH dependent T_1-MRI contrast agent†

†Electronic supplementary information (ESI) available. See DOI: 10.1039/c9nr10397j

Bo Chen‡,[a]

‡These authors contributed equally.

Zhanhang Guo‡,[b]

Chunxian Guo,[a]

Yu Mao,[b]

Zhiguo Qin,[b]

Dewen Ye,[b]

Zang Fengchao,[c]

Zhichao Lou,[d]

Zuoheng Zhang,[b]

Mingyue Li,[e]

Yanlong Liu,[f]

Min Ji,[b]

Jianfei Sun,[b]

Ning Gu*,[b] ORCID: 0000-0003-1438-5629

[a]Materials Science and Devices Institute, Suzhou University of Science and Technology, 1 Kerui Road, Suzhou 215009, Jiangsu, China.

[b]Jiangsu Key Laboratory for Biomaterials and Devices, Department of Biological Science and Medical Engineering, Southeast University, Nanjing 210009, P. R. China. Email: guning@seu.edu.cn

[c]Jiangsu Key Laboratory of Molecular and Functional Imaging, Medical School, Southeast University, Nanjing 210096, P. R. China.

[d]College of Materials Science and Engineering, Nanjing Forestry University, Nanjing 210037, China.

[e]Institute of Medical Devices (Suzhou), Southeast University, Suzhou 215163, Jiangsu, China.

[f]Research Institute of Chia Tai Tian Qing Pharmaceutical Group Limited by Share Ltd, Nanjing 210000, China.

Abstract

Iron based nanomedicine (IBNM) has been one powerful diagnostic tool as a magnetic resonance imaging (MRI) contrast agent (CA) in the clinic for years. Conventional IBNMs are generally employed as T_2-MRI CAs, but most of them are constrained in clinical indication expansion by magnetic susceptibility artifacts. In comparison, extremely small iron oxide (ESIO) with a core size less than 5 nm has demonstrated the T_1-MRI effect, which provides prospects for a Gd-based agent alternative. Nevertheless, currently developed ESIOs for T_1-MRI CAs always require harsh conditions such as a high temperature and high boiling point reagent. Moreover, very few of the currently developed ESIOs meet the stringent pharmaceutical standard. Herein, on the basis of a crystal nuclear precipitation–dissolution equilibrium mechanism and outer/inner sphere T_1-MRI theory, monodisperse ESIOs with an average size of 3.43 nm (polydispersity index of 0.104) are fabricated using a moderate cooling procedure with mild coprecipitation reaction conditions. The as-synthesized ESIOs display around 3-fold higher T_1 MRI signal intensity than that of commercial Ferumoxytol (FMT), comparable to that of Gd-based CAs *in vitro*. Additionally, the T_1-MRI performance of the ESIOs is pH dependent and delivers bright signal augmentation. Eventually, the internalization into mesenchymal stem cells of the ESIO is realized in the absence of a transferring agent. Considering the identical structure and composition of the ESIOs as compared to that of FMT, they could meet the pharmaceutical criteria, thus providing great potential as T_1-MRI Cas, for instance as stem cell tracers.

Introduction

As the most successful developed inorganic metal nanomedicine so far, iron based nanomedicine (IBNM) has been approved vastly in the clinical medical realm, including magnetic hyperthermia, iron supplements, magnetic separation and so forth, thanks to the prominent magnetic responsiveness and biosecurity in the human body.[1–3] Ferumoxytol (FMT) is currently the only IBNM active on the market by official permission for anaemia treatment. Moreover, FMT serving as an “off-label” model drug has attracted great attention in new clinical applications such as tumour therapy,[4,5] stem cell therapy,[6–8] transplanted stem cell tracking and so on,[9–11] and magnetic resonance imaging contrast agents (CAs) play the most significant part therein. MRI CAs are generally divided into T_1-MRI CAs for shortening the longitudinal relaxation time of water protons (brighter images) and T_2 ones for shortening the transverse relaxation time (darker images).[5] Gd-Based CAs dominate T_1-MRI clinical applications, whilst Gd^{3+} ion leakage, deposition and short circulation life are the bottlenecks.[12,13] Classical iron based MRI CAs with superparamagnetism mainly demonstrate the T_2-MRI effect, including Feridex® and Resovist® approved in the clinic, which is associated with magnetic susceptibility artifacts, peripheral region confusions, background interference and relatively low resolution.[14–16]

To solve these issues discussed above, recent efforts have been focused on the development of T_1 iron based MRI.[3] The size-dependent magnetic properties of iron oxide nanoparticles have been reported, and extremely small iron oxide (ESIO) with crystal size below 5 nm exhibited good T_1-MRI performance.[13,17–20] However, current ESIO preparations mainly require harsh conditions such as high temperature and high boiling reagents.[12–14,21] Besides, most of the products do not fulfil pharmaceutical demand, and thus it is difficult to realize their application *in vivo*. IBNM scale-up production generally adopts chemical coprecipitation due to the reproducibility and low-toxic nature of the process, which readily reaches the pharmaceutical standard.[22,23] The coprecipitation typically involves the following steps: $Fe(OH)_3$ and $Fe(OH)_2$ are respectively produced in a basic environment from an iron salt aqueous solution, then $Fe(OH)_3$ reacts with $Fe(OH)_2$ to generate the Fe_3O_4 crystal seed, which precipitates out when supersaturated and grows.[24] But, it is well known that irregular particle shapes and broad size distributions generally occur in the common coprecipitation, resulting from the association of crystal nuclear precipitation with the particle expanding growth stage. Many endeavours have been devoted to improving common precipitation by focusing on the nucleation and growth stage.[25–27]

In our previous study,[28] low temperature was discovered to offer nuclear formation and crystal growth in a more ordered and controllable step compared to the typical coprecipitation procedure. Particularly, low temperature may have an influence on the homogenous nucleation of the metal crystal, and may confine the nuclear sharp growth.[29–31] A cooling process is thus considered to enable ESIO production based on a crystal nuclear precipitation–dissolution equilibrium mechanism. Furthermore, different from the ultrahigh temperature reaction, cooling coprecipitation is readily controllable in a long-term process and can avoid drastic changes in the reaction. Besides, other optimal operation factors including coating materials and pH modulation can also be easily integrated into this process for better T_1-MRI performance, according to the classical outer/inner sphere MRI model.

In this study, we present a moderate cooling preparation strategy for the synthesis of monodispersed extremely small iron oxide (Fig. 1). Fe_3O_4 nucleation and growth are tuned by starting temperature, cooling rate and so forth. ESIO coated by polyglucose sorbitol carboxymethylether (PSC) with good biosafety and prominent T_1 MRI performance is eventually obtained. The role of initial temperature, cooling rate,

coating material and pH in the T_1-MRI behaviour of the ESIO is investigated. The T_1-MRI signal intensity is quantified and compared with that of commercial FMT *in vitro* and *vivo*. In addition, the stem cell label and imaging performance of ESIO is assessed.

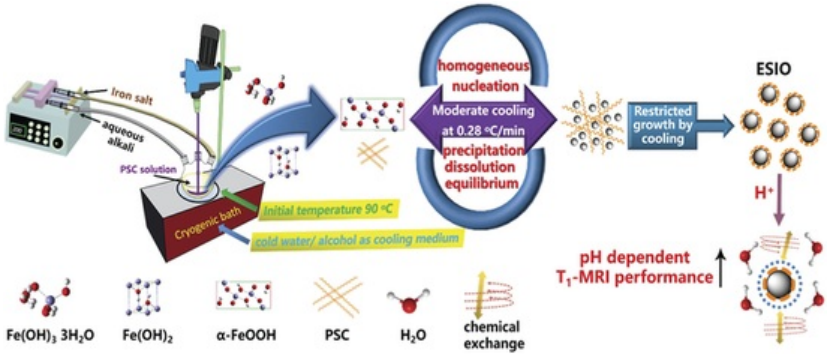

Fig. 1 Schematic illustration of the moderate cooling coprecipitation approach for the synthesis of ESIO.

Results and discussion

Investigation into the effect of different initial temperatures on the T_1-MRI performance of ESIO

Generally speaking, low temperature preparation may cause insufficient crystal growth and inferior quality, whilst high temperature may induce tiny crystal assembly, so the selection of initial temperature was important. Thereby, different starting temperatures of 90 °C, 60 °C and 30 °C were set, respectively. Then, the solution was cooled down in a cryogenic bath, and the temperature of the cryogenic bath was changed in steps of 10 °C. The time at each temperature point was recorded, and the temperature decline rate was calculated (about 0.28 °C min^{-1}). Additionally, in order to ensure that ESIO has the identical composition to that of FMT, the attached material of FMT was selected as the ESIO coating ingredient, which is one kind of dextran T10 derivative called polyglucose sorbitol carboxymethyl ether (PSC). The materials or reagent addition conditions including PSC/Fe salt ratio and concentration were maintained the same as that of common commercial FMT production.[25,28] On the other hand, to avoid fast nucleation and growth, the initial ammonia and iron salt solutions were equiproportionally diluted, and mixed into the PSC solution at a rather slow speed with a microinjection pump.

TEM images (Fig. S1†) manifested that sample cooling from 60 °C merely formed larger particles in very low concentration, whereas cooling from 30 °C resulted in particles with irregular shapes and in low yields. Both of them are worse than the sample obtained by cooling from 90 °C (Fig. 2b) based on size and distribution, which may be due to the cooling temperature range. The long period of cooling process from the high temperature of 90 °C provides a complete crystal nucleation stage. Meanwhile, the suitable PSC amount combined with cooling operation avoids tiny crystal aggregation and restricts excessive growth. As a consequence, 90 °C was set as the optimal initial temperature.

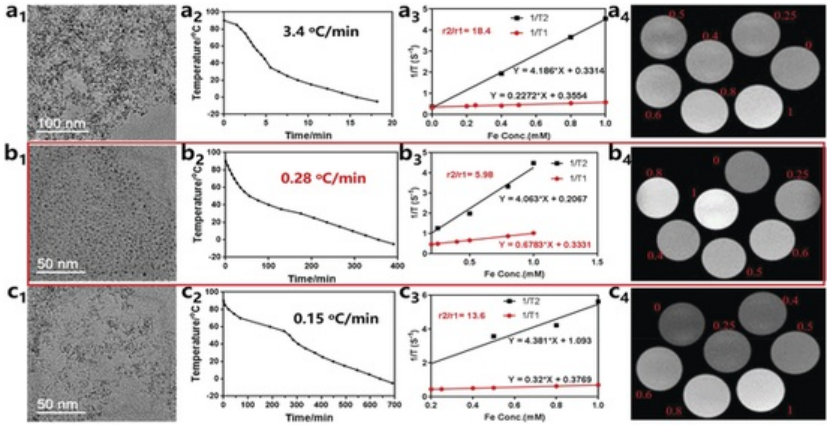

Fig. 2 TEM images, time dependent reaction cooling plot, Fe concentration dependent longitudinal relaxation time reciprocal curve and T_1-weighted MR phantom images of ESIO obtained with cooling rates of (a) 3.4 °C min^{-1}, (b) 0.28 °C min^{-1}, and (c) 0.15 °C min^{-1} all from the initial temperature of 90 °C.

Investigation into the effect of different cooling rates on the T_1-MRI performance

From the above results, it is clear that initial temperature plays a significant role in supersaturation variation, further acting on the crystal size. The equilibrium critical radius (r^*) of a nucleated crystal is given by eqn (1):[32]

$$r^* = \frac{2v\sigma}{kT \ln S} \quad (1)$$

where v, σ and k represent the crystal surface energy, molecular volume of the precipitated embryo and Boltzmann constant, T is the temperature and S is the solution supersaturation, which is defined as the difference value between the solute concentration and the solubility at a specified temperature. If the radius is beyond r^*, nucleation will occur and tiny particles will form. The constant r^* will be obtained when the variation of v keeps the same pace as the T and S variation. The relationship of crystal surface energy and supersaturation complies with eqn (2) as below:[33]

$$\Delta\mu = \mu_l - \mu_c = \frac{2\sigma v}{h} \quad (2)$$

where $\Delta\mu$ is the solution supersaturation, v denotes the volume of a single growth unit, σ represents the surface energy of the crystallites, h is the distance from the crystallite's center to its surface, and l and c represent the solution and crystal phases, respectively. Thereby, if T and S both decrease in a moderate manner while v reduces as S declines, a cooling process may occur with a small and constant r^*.

Based on the above analysis, an appropriate cooling rate is regarded as crucial in iron oxide crystal seed precipitation. It can be inferred that if S and v. decrease while T declines, homogenous nucleation would occur. Specifically, depending on the set temperature and cooling media (cooling water and ethanol), the rate of 3.4 °C min^{-1}, 0.28 °C min^{-1}, and 0.15 °C min^{-1} is calculated and applied in the subsequent cooling operation, respectively. 3.4 °C min^{-1} is obtained when the cryogenic bath temperature is set at −20 °C. The medium cooling rate of 0.28 °C min^{-1} is achieved by setting a moderate temperature of the cryogenic bath, changing with every 10 °C decreasing step. 0.15 °C min^{-1} is attained by setting the temperature in the cryogenic bath with every 5 °C decreasing step.

As shown in the TEM images, only using the rate of 0.28 °C min^{-1} achieves the optimal uniform particle distribution with extremely small size (Fig. 2b$_1$), whereas the 3.4 °C min^{-1} rate causes conspicuous large-scale aggregation (Fig. 2a$_1$), and the sample formed at 0.15 °C min^{-1} displays good dispersion but a larger crystal size of around 10 nm (Fig. 2c$_1$). It can be interpreted that rapid cooling facilitates small crystal aggregation (3.4 °C min^{-1}), and slow cooling promotes nuclear growth into larger particles (0.15 °C min^{-1}). As for the relaxometric property measurement (Fig. 2a$_3$, b$_3$ and c$_3$), the sample formed at the moderate cooling rate of 0.28 °C min^{-1} exhibits the best T_1-MR signal intensity, with the highest longitudinal relaxation rate (r_1) value (0.68 mM^{-1} s^{-1}) and the lowest transverse/longitudinal relaxation rate (r_2/r_1) value (5.98) among these three samples. Furthermore, iron oxide nanoparticles prepared at high Fe and PSC concentrations were prepared for comparison. The TEM images validated that the 0.28 °C min^{-1} cooling rate is optimal for the size distribution as well (Fig. S2†). Although the size increased, the particles demonstrated a regular morphology and uniform distribution after moderate cooling at 0.28 °C min^{-1}, which coincides with the results shown in Fig. 2. Hence, it is evident that cooling from 90 °C at the moderate rate of 0.28 °C min^{-1}, forming the sample named ESIO-1, is the most effective route to attain ESIO with a uniform dispersion and optimal T_1-MRI behaviour (Fig. 2b$_4$).

Investigation into the effect of the coating material on the T_1-MRI performance

In spite of realizing size control, the T_1-MRI effect of ESIO-1 was unsatisfactory. For a successful T_1-MRI CA, high r_1 and low r_2/r_1 values are required. Based on the classical outer/inner sphere model (eqn 3 and 4 are given in the ESI[†]),[34,35] in order to obtain an optimal T_1-MRI CA, spin interaction with the vicinity water proton should be further elevated based on a small size crystal.[18,36] Next, the regulation of particle surface properties should be performed. Given the long flexible chain of PSC, a plethora of a PSC formed thick layer with a high packing density outside the iron oxide crystal, interface polarization and interface chemical exchange may be immensely attenuated.[37–39] Thereby, we speculate that removing the coating material might be beneficial to T_1-MRI elevation. Then, naked ESIO absent of PSC was synthesized following the above process without the PSC addition. As anticipated, the naked iron oxide nanoparticles perform better in T_1-MRI (Fig. S3[†]) than those coated by PSC, even though aggregation occurred due to the lack of surface modification. The structural property comparison of the naked iron oxide nanoparticle and ESIO-1 is displayed in Fig. 3. AFM images (Fig. 3a and d) and hydrodynamic measurement (Fig. 3b and e) both present minor aggregation of the naked particles. Besides, the polydispersity index (PDI) value of 0.279 of the naked iron oxide nanoparticles is higher than 0.120 of ESIO-1, indicating that the former show an inferior particle distribution. Furthermore, the colour of the samples observed at different temperatures changed to dark yellow gradually (Fig. 3c and f), further confirming the particle size expansion as temperature decreases. Based on the results, apart from the size and morphology contributions, it is well-known that particle surface properties indeed play a crucial role in T_1-MRI performance.[12,40] The T_1 relaxation enhancement of the naked iron oxide stems from the increasing amount of Fe^{3+} exposed on the particle surface interacting with the surrounding water proton H^+. PSC with a negative charge stacking on the iron oxide crystal surface may extend the impact distance, consequently attenuating the spin perturbation.

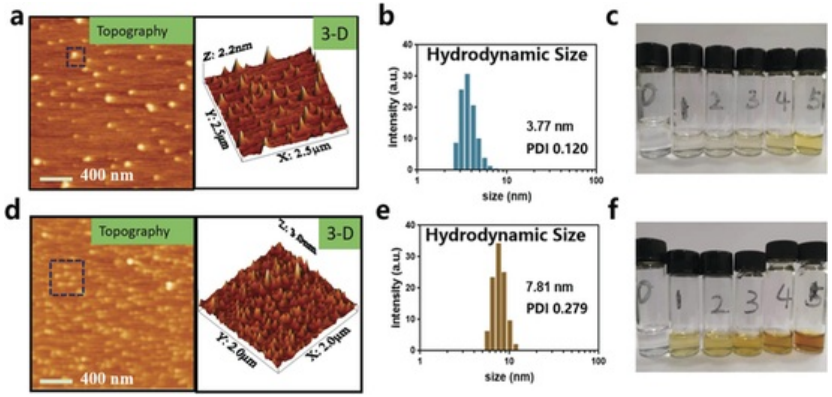

Fig. 3 AFM images of (a) ESIO-1 and (d) naked ESIO. Hydrodynamic size of (b) ESIO-1 and (e) naked ESIO. The photos of samples taken at each 5 °C decrease corresponding to (c) ESIO-1 and (f) naked ESIO (the sample bottles are placed from left to right in time order).

Investigation into the effect of pH on the T_1-MRI performance

Notably, considering the stability and long-term application *in vivo*, moderate surface modification by PSC is indispensable. Additional measurement must be performed to augment the chemical exchange interaction in the presence of PSC. It has been reported that Gd-dots and $NaGdF_4$ nanodots by special material modification exhibit ultrasensitive MRI effects, benefiting from increased hydrogen bonding and paramagnetic Gd^{3+} ion concentration.[41,42] In our experiment, the alkaline aqueous solution of ESIO containing a high concentration of OH^- may also alleviate the Fe^{3+} function, thus down-regulating pH should be preferred. ESIO-1 forms in a weakly acidic solution at a pH of 6.10. For the deep investigation of the pH effect, a series of ESIO solutions with gradient-varying pH values was thus prepared with the interval of about 1–2. Therefore, pH values of around 8, 5, 4 and 3 were set, respectively. T_1-MR phantom images are shown in Fig. S4 and S5,[†] based on which the relaxivity evaluation was carried out. As the pH decreases from 8.01 to 4.94, the r_2/r_1 ratio declines from 10.98 to 1.93 (red plot in Fig. 4a), and zeta potential increases from −37 mV to 18.9 mV (black plot in Fig. 4a). So, it was found that pH and zeta potential seem to have a close correlation with T_1 MR relaxation behaviour. Exceptionally, when pH reduces continuously to 3.03 and 2.73, r_2/r_1 rises conversely. Given the neutral pH *in vivo*, ESIO formed at pH 3.03 and 2.73 is unsuitable for long-term use, due to the instability in strong acidic environments. The possible iron oxide decomposition of ESIO at pH 3.03 under acidic conditions is shown in Fig. 4f with the indistinct morphology of the particles. Therefore, the CA candidate was chosen from the samples of pH above 4.94. *Via* extracting the grey value from the MR phantom images, the T_1-MRI signal intensity of the samples was obtained and it is presented in Fig. 4b; the signal intensity increases with H^+ concentration elevation, and ESIO formed at pH 4.94 is the brightest one, being approximately 3-fold stronger than that of the FMT group (Fig. S5d[†]) at the equivalent iron concentration. As shown in the TEM images (4c–e), ESIO maintains a monodisperse state (PDI values remain between 0.1 and 0.15) even though pH changes; iron oxide core size (2.83 nm) and hydrodynamic diameter (3.43 nm) also remain nearly constant, showing that ESIO is completely stable in a weakly acidic environment. In accordance with the pH variation, the r_1 value (altering from 0.0534 to 3.93 at 7 T) and r_2/r_1 ratio (altering from 10.98 to 1.93 at 7 T) showed a remarkable improvement, and the relaxation parameters of ESIO formed at pH 4.94 (Fig. 4c) are comparable to

those of DTPA-Gd (Fig. S5c[†]), suggesting its great potential as a clinical T_1-MRI CA *in vivo*.

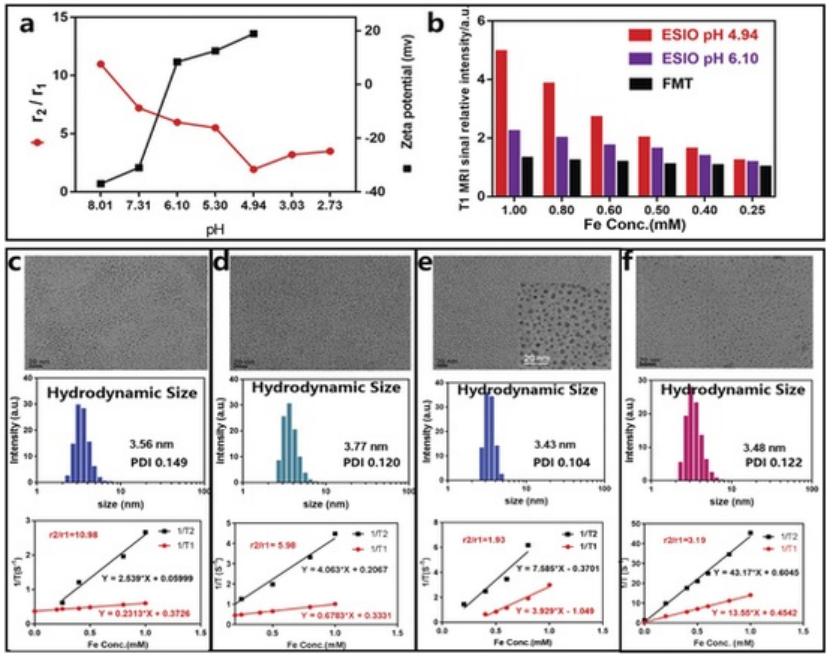

Fig. 4 (a) The plot of r_2/r_1 and zeta potential varying with pH value; (b) T_1-MRI signal intensity comparison of ESIO formed at pH 4.94, ESIO formed at pH 6.10 and FMT. TEM images, hydrodynamic size and Fe concentration dependent relaxivity curves of (c) ESIO formed at pH 8.01, (d) ESIO formed at pH 6.10, (e) ESIO formed at pH 4.94 and (f) ESIO formed at pH 3.03.

Structure, composition and magnetic property analysis

The iron based part of ESIO is composed of magnetite inverse spinel crystal (JCPDS: 39-1346), with the characteristic XRD peaks shown in Fig. 5a. The peaks located at 30.3, 35.6, 43.6, 53.4, 57.4, 63.1 and 70.9 are assigned to the (220), (311), (400), (422), (511), (440) and (533) crystal phases separately, which is consistent with the diffraction peaks of FMT.[28,43] Notably, the diffraction peak intensity and pattern smoothness decrease as the particle diameter reduces, reflecting that the crystallinity of ESIO is worse than that of FMT. It is comprehended that a small size and low crystallinity will result in paramagnetism and low magnetization of the particle for T_1-MRI. The hydrodynamic diameter of ESIO was recorded over 7 days (Fig. 5b), and consistent with the TEM results shown in Fig. 4c–e, the subtle negligible changes demonstrate that the particles could remain in a stable state in the stock solution for a long period, ensuring that the subsequent experiment *in vitro* or *vivo* can be finished in one week. The sample structure composition was further validated by using FT-IR absorption spectra (Fig. 5c), and the bands at 1000 cm^{-1} and 580 cm^{-1} can be assigned to the ether-oxygen covalent bond stretching vibration of PSC and iron oxide distinctive absorption, respectively, indicating the presence of PSC outside the iron oxide particles by –C═O coordinating with Fe^{3+}, and offering sufficient medicinal security for ESIO. The as-prepared ESIO above all exhibits the signature of paramagnetism with weak magnetic responsive performance. It is readily seen that both saturation magnetization (Fig. 5d) and magnetic susceptibility values (Fig. 5e) of ESIO are far less than that of superparamagnetic FMT. ESIO formed at pH 4.94 has the lowest saturation magnetization and FMT has the highest one. The zero field/field cooling curve measured by PPMS (Fig. 5f) further affirmed the paramagnetism of ESIO and superparamagnetism of FMT, in line with the detection results of VSM. These results comply with the aforementioned spin canting theory, which is determined by particle size. The paramagnetic property of ESIO formed at pH 4.94 indicates its great potential as a T_1-MRI CA, rather than the T_2 type property that FMT exhibits. The structural composition and T_1 relaxation parameter comparison of several typical iron based T_1-MRI CAs is listed in Table 1; ESIO formed in our work is fully qualified to act as a T_1-MRI CA with excellent r_1 and r_2/r_1 values even at a high magnetic field intensity.

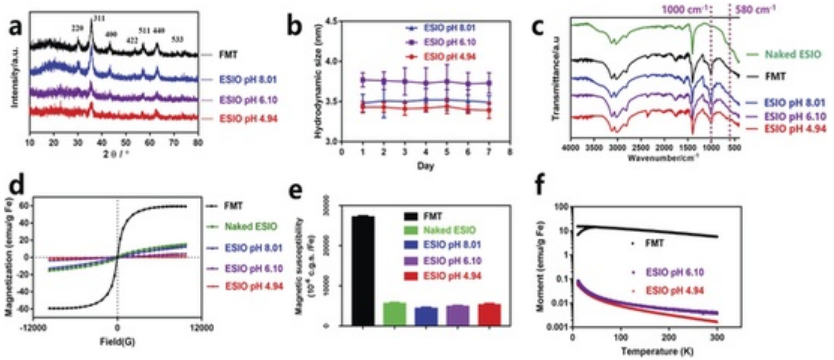

Fig. 5 (a) XRD patterns of ESIOs and FMT. (b) Hydrodynamic diameter measurement of ESIOs over 7 days. (c) FT-IR spectra of ESIOs and FMT marked with the characteristic peaks. (d) Field-dependent magnetic hysteresis loop of ESIOs and FMT. (e) Magnetic susceptibility measurement of ESIOs and FMT. (f) Zero-field cooling and field cooling curves of ESIOs and FMT (H = 100 Oe).

Table 1 Structure composition and magnetic resonance relaxation parameter comparison of several typical iron based T_1-MRI contrast agents

Synthetic method	Product name	Structure composition	Core size/overall size (nm)	$r1$ (mM^{-1} s^{-1})	$r2$ (mM^{-1} s^{-1})	$r2/r1$ (magnetic field strength)
Thermal decomposition	ZES-SPIONs[13]	Zwitterionic dopamine sulfonate grafting on γ-Fe_2O_3	3/4.4	1.5	17	11.00 (7 T)
	ESIONs[12]	PO-PEG coating Fe_3O_4	3/15	4.77	29.2	6.12 (3 T)
Polyol method	Ultrasmall PEGylated INOPs[47]	HOOC-PEG-COOH coating Fe_3O_4	5.4/10.1	19.7	39.5	2.00 (1.5 T)
	Ultra-small Fe_3O_4 [48]	Trisodium citrate grafting on Fe_3O_4	1.9/—	1.415	2.87	2.03 (7 T)
Redox reaction	FeOOH/WMSN-PEG[49]	α-FeOOH loaded in mesoporous silica NPs	2–3/—	4.03	7.94	1.97 (4.7 T)
Solvothermal method	GP-MNPs[50]	Glycopeptide grafting on Fe_3O_4	8.3 ± 2/15.5	16	62	3.9 (1.5 T)
Ion chelation	Fe^{3+}-MelNPs[51]	PEG-MelNP chelate with Fe^{3+}	—/98	17	18	1.10 (3 T)
High temperature injection	ES-MION3 [14]	PAA modifying on Fe_3O_4	3.6/—	8.8	22.7	2.58 (1.5 T)
	VSOP[52]	Citric acid modifying on Fe_3O_4	4/8.6	8	34	4.25 (3 T)
Moderate cooling precipitation	**ESIO this work**	**PSC coating Fe_3O_4**	**2.83/3.43**	**3.93**	**7.59**	**1.93 (7 T)**

To sum up, the T_1 MRI enhancement can be elucidated by the following behaviour: ① surface spin canting effect augmentation with particle size reduction; ② chemical exchange acceleration between coordination water proton and paramagnetic Fe^{3+} exposure on the surface with pH reduction.[10]

T_1-MRI effect evaluation *in vitro*

Prior to detecting the T_1-MRI effect in mesenchymal stem cells (MSCs), cytocompatibility assessment of ESIO formed at pH 4.94 was performed by using the MTT test. After 24 h incubation, ESIO exerts little negative impact on MSCs similarly to FMT based on counting the OD value (Fig. 6a), even when Fe concentration reaches 1000 μg mL^{-1}. The excellent cytocompatibility may derive from the mild coprecipitation process and PSC modification. The iron oxide nanoparticle label amount in the MSCs observed as Fe concentration is shown in Fig. 6b. In a conventional procedure, FMT needs mixing with a cationic ion transfection reagent such as polylysine (PLL) for efficient labelling in MSCs. Iron based nanoparticles mainly take advantage of the high surface positive charge provided by a transfection agent to promote fusion into the cell membrane.[44–46] As shown in Fig. 6b, FMT indeed requires PLL wrapping to achieve effective uptake. But surprisingly, the single ESIO without PLL addition succeeds in sufficient labelling in the MSCs. At the same time, PLL addition seemingly has little impact on the label amount.

To the best of our knowledge, the stem cell is so fragile that an exogenous reagent will always disturb its subsequent fate including proliferation and differentiation. Thereby, the labelling capacity free of a transfection agent is commendable for the ESIO. The T_1-MRI result of ESIO in the MSCs well matches with the label content in the stem cell (Fig. 6c–f). Prominent brightness augmentation is present in the MSC pellets labelled by the single ESIO without a transfection agent (Fig. 6c). To obtain a distinct contrast, MSCs labelled by FMT and FMT + PLL even become dark at high Fe concentrations possibly due to the large particle agglomeration (Fig. 6e and f), in good agreement with the sample MRI test in aqueous solution. Gratifyingly, the discoveries confirm that the as-obtained ESIO can be effectively transferred into MSCs with no aid of a transfection reagent, and can present a distinctive T_1 enhancement signal in MSCs. The positive charge enables ESIO to fuse with the cell membrane surface of negative charge, and the extremely small size additionally promotes particle endocytosis into the cell. The special labelling profile renders the ESIO formed at pH 4.94 as a promising stem cell tracking agent *in vivo*.

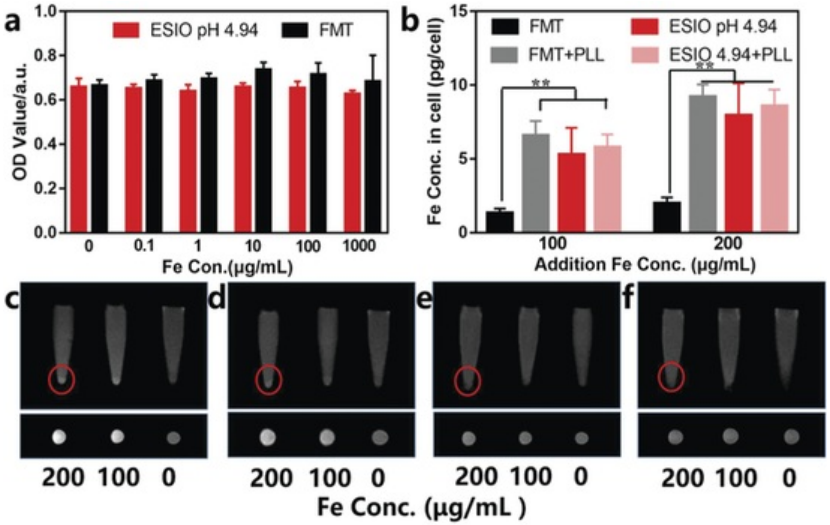

Fig. 6 (a) MTT test after incubation with ESIO formed pH 4.94 and FMT at different Fe concentrations. (b) ICP-MS measurement of Fe content in MSCs labelled by ESIO formed at pH 4.94, ESIO formed at pH 4.94 + PLL, FMT and FMT + PLL with different Fe addition concentrations (200 and 100 μg mL^{-1} Fe). Error bars indicate standard deviation, $^{**}P < 0.01$, $n = 3$. T_1-Weighted MR images of MSC pellets after 24 h incubation with (c) ESIO formed at pH 4.94, (d) ESIO formed at pH 4.94 + PLL, (e) FMT + PLL and (f) FMT with different Fe addition concentrations (200, 100 and 0 μg mL^{-1} Fe).

T_1-MRI effect evaluation in rat brain and abdominal regions

The feasibility of ESIO for MRI *in vivo* was assessed based on the MRI results *in vitro*. T_1 MR anatomical images *in vivo via* brain microinjection are exhibited in Fig. 7a–d (the microinjection points are highlighted by a red dotted circle and arrow). In contrast to the MRI images before injection (Fig. 7a), the FMT group demonstrates no bright signal augmentation in the local administration region (Fig. 7b), whilst the ESIO group displays extraordinary T_1-MRI intensity enhancement in the local region. As anticipated, the signal brightness increases distinctively as the pH of the sample reduces (Fig. 7c and d), coincident with the MRI performance *in vitro* (Fig. 6). For explicit comparison and refined quantitative analysis, the targeted area grey value was extracted from the anatomical images as the Δ signal-to-noise (ΔSNR) ratio, calculated by eqn (6) and (7) listed in the ESI.[†] Evidently, ΔSNR of the brain injection region increases from 26.5% for FMT to 102.4% for ESIO formed at pH 6.10, and the maximum 141.1% for ESIO formed at pH 4.94 (Fig. 7g). Both ESIOs show a highly significant difference in T_1 MRI signal compared to that of FMT. As another comparison *in vivo*, T_1 MR anatomical images of rat abdomen upon subcutaneous injection are also listed (the injection points are highlighted by a red circle). ESIO formed at pH 6.10 causes the MR signal of the injection region to be immensely brighter than that before injection (Fig. 7e), and ΔSNR is 89.8% (Fig. 7h), opposite to that of the images in the normal subcutaneous issue before injection. Furthermore, ESIO formed at pH 4.94 generates a tremendously strong signal (Fig. 7f) with ΔSNR up to 173.5% (Fig. 7h), showing the highly significant difference to the intensity of ESIO formed at pH 6.10. These results all validate that ESIO has excellent pH dependent T_1 MRI performance *in vivo*, establishing a solid basis for MRI application in the clinic.

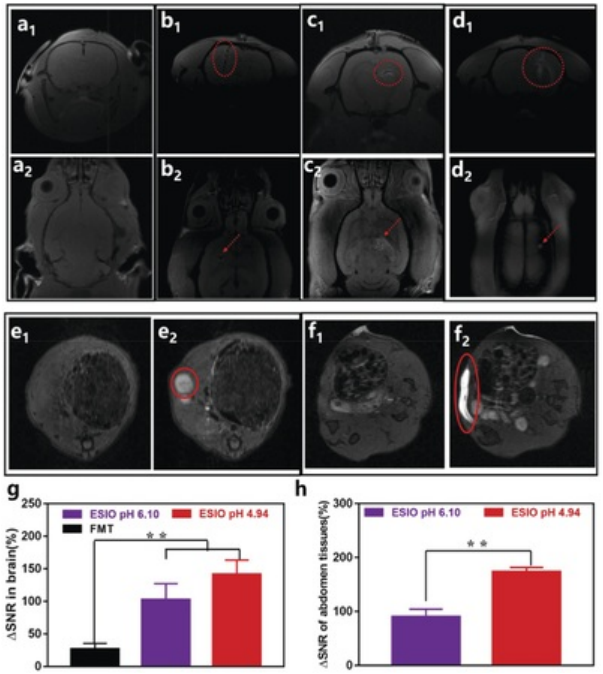

Fig. 7 T_1-Weighted MR images of rat brain: (a_1) before injection cross section and (a_2) coronal slice. T_1-Weighted MR images of rat brain: (b_1) 8 h after FMT microinjection cross section and (b_2) coronal slice. T_1-Weighted MR images of rat brain: (c_1) 8 h after microinjection of ESIO formed at pH 6.10 cross section and (c_2) coronal slice. T_1-Weighted MR images of rat brain: (d_1) 8 h after microinjection of ESIO formed at pH 4.94 cross section and (d_2) coronal slice (0.2 mg Fe per kg, 15 μL). T_1-Weighted MR images of rat abdominal subcutaneous regions (cross section slice): (e_1) pre-injection and (e_2) 30 min after injection of ESIO formed at pH 6.10; (f_1) before injection and (f_2) 30 min after injection of ESIO formed at pH 4.94 (3 mg Fe per kg). (g) T_1-MRI ΔSNR histogram of rat brain after FMT and ESIO administration. (h) T_1-MRI ΔSNR histogram of rat subcutaneous abdominal region after two ESIO administrations. Error bars indicate standard deviation, $*P < 0.05$, $**P < 0.01$, $n = 3$.

Conclusion

In summary, we present a chemical co-precipitation strategy that implements a mild and controllable cooling procedure to enable homogenous nucleation and restricted slow growth for the synthesis of monodispersed ESIO. The monodispersed ESIO displays a much better pH dependent T_1 MRI enhancement. Moreover, the ESIO exhibits much better stem cell labelling capacity than conventional FMT. It was found that the extremely small size, uniform distribution and surface positive charge properties of the ESIO play essential roles in the enhanced T_1-MRI performance. It is worth noting that the shortening of ESIO longitudinal relaxation time may originate from the improved chemical exchange between water protons and iron oxide crystals. As for the pharmacokinetics of ESIO in our work, it may be predicted based on that of Ferumoxytol with a similar structural composition. ESIO with a smaller size can escape uptake by the mononuclear phagocytic system (MPS) after circulation in the veins, rapidly enter the kidneys and metabolize out of the body, thereby shortening the circulation time *in vivo*, which is opposite to the fate of Ferumoxytol. The strategy presented here provides a new insight into iron based nanomaterial preparation, and also enriches the technologies for production of extremely small iron oxide nanomedicine. The produced ESIO could be used in clinical application as a T_1-MRI CA and stem cell tracer, motivating the development of magnetic nanomedicine in clinical translation.

Experimental section

Materials and methods

The materials and reagents such as ferric chloride, ferrous chloride, ammonium aqueous solution (28%), NaOH solid and HCl aqueous solution (12 M) used in the experiments are all of chemically pure grade. PSC (the coating material of Ferumoxytol) and FMT were prepared in our lab and pharmaceutical items were verified by Chiatai Tianqing Pharmaceutical Group Co., Ltd. Mesenchymal stem cells (MSCs) was obtained from the Stem cell lab of Drum Tower Hospital in Nanjing. Healthy male rats (Wistar, 5-weeks-old) were purchased from the college of veterinary medicine, Yangzhou University. All the animal experiments were performed in strict accordance with the Animal Research: reporting of *in vivo* experiments guidelines and were approved by the Institutional Animal Care and Use Committee at the Medical School of Southeast University (Nanjing, China).

Synthesis of extremely small iron oxide (ESIO) by moderate cooling coprecipitation from different initial temperatures of 90 °C, 60 °C and 30 °C

PSC (800 mg, 0.08 mM) was dissolved in ultrapure water (10 mL), and ferric chloride hexahydrate (600 mg, 2.2 mM) and ferrous chloride tetrahydrate (300 mg, 1.5 mM) were dissolved in another sample of ultrapure water (5 mL). The two solutions above were mixed in a three-neck bottle, then stirred vigorously (300 rpm) with nitrogen gas bubbling, and the bottle was immediately placed in a water bath (90 °C, 60 °C or 30 °C). An optical fiber probe was inserted into the solution for temperature monitoring. Then, ammonium aqueous solution (28%, 900 μL) was added *via* a dual-channel microinjector (100 μL min^{-1}) with violent stirring (800 rpm). Thereafter, heating and stirring were terminated, and the bottle was transferred to a cryogenic bath containing cold water, ice water and ethanol in order until cooling to −5 °C. The temperature decline rate was calculated as 0.28 °C min^{-1}. ESIO was eventually obtained after workup by dialysis and filtration.

Synthesis of ESIO by moderate cooling coprecipitation with different cooling rates

Ferric chloride hexahydrate (50 mg, 0.18 mM) and ferrous chloride tetrahydrate (18.4 mg, 0.09 mM) were dissolved in ultrapure water (250 mL). The iron salt solution was placed in hot water (90 °C) with vigorous stirring. Then, ammonium aqueous solution (50 μL of 28% $NH_3 \cdot H_2O$ in 10 mL of water) was injected (200 μL min^{-1}) under a nitrogen atmosphere for about 20 min. PSC solution (10 mL, 0.005 mM) was subsequently introduced with stirring. 2 min later, heating and stirring were terminated, the bottle was transferred into a low temperature medium bath, and the solution was cooled with the declining rate of 3.4 °C min^{-1}, 0.28 °C min^{-1}, or 0.15 °C min^{-1} separately until the temperature decreased to −5 °C. In addition, the solution was sampled (1 mL) each 5 °C during the cooling process for other characterization.

Synthesis of ESIO by moderate cooling coprecipitation with no coating materials

The naked ESIO absent of PSC was synthesized following the procedure above except without the PSC addition.

Synthesis of ESIO by moderate cooling coprecipitation with pH tuning

The solution for ESIO-1 had a pH of 6.10 and can be regarded as a weak acid. ESIO solutions with other different pH values (8.01, 7.31, 5.30, 4.94, 3.03 and 2.73) were tuned by using 6 M HCl or 6 M NaOH addition into the ESIO-1 solution correspondingly.

Characterization of as-synthesized ESIOs

The morphology and size of the iron oxide core were visualized by using TEM (JEM-2100/FEI, Technai G20). The hydrodynamic diameter and zeta potential were measured by using a size and potential analyser (Malvern, NanoZS90). The particle size was studied by using AFM (5500, Agilent). The crystal parameters were obtained from X-ray diffraction patterns (X'TRA, ARL) in the 2θ range of 10°–80°. IR spectra were recorded on a FT-IR spectrometer (IRAffinity-1, Shimadzu). Iron content was detected by inductively coupled plasma mass spectrometry (Optima 5300DV, PE) and UV-Vis spectrophotometry (UV-3600, Shimadzu, Japan). The temperature variation curve was recorded by an optical fibre thermometer (FISO UMI 8, Canada). The fluorescence intensity of the MTT test was recorded by a microplate reader (Infinite 200PRO). Magnetic susceptibility was measured by a magnetic susceptibility balance (Sherwood, MK1). Magnetic hysteresis loops and saturated magnetization were obtained by using a vibration sample magnetometer (7407, LakeShore) at room temperature. Field cooling and zero-field cooling curves were recorded by a PPMS-9 (Quantum Design). The MRI test was carried out by using a small animal MR scanner (7T, PharmaScan, Bruker) and MR scanner (3T, Verio, Siemens).

MRI and relaxometric property test of ESIO *in vitro*

A sample test solution (5 mL) was prepared with different Fe concentrations of 1 mM, 0.8 mM, 0.6 mM, 0.5 mM, 0.4 mM, and 0.25 mM in plastic tubes, respectively, by diluting the original sample solution in order. These tubes were placed into the MRI scanner coil center, and T_1/T_2 phantom images were recorded with the corresponding sequence shown in the ESI;[†] T_1/T_2 relaxivity parameters were also measured.

Cytotoxicity test of the ESIO

The thiazolyl blue tetrazolium bromide (MTT) assay was firstly implemented for cytocompatibility evaluation. MSCs (5×10^3, 100 μL) were seeded onto a culture dish and grown for 24 h. Then, mesenchymal stem cells

(MSCs) were incubated with ESIO and FMT at different Fe concentrations overnight (0.1, 1, 10, 100, and 1000 μg ml^{-1}). Thereafter, the culture medium was replaced with new media (100 μL) and MTT (10 μL). 4 h later, the medium was removed and the dissolved formazan was precipitated in DMSO. Cell viability was assessed by recording the absorbance at 450 nm as OD values with a microplate reader.

ESIO labelling in stem cells and MRI test *in vitro*

ESIO or FMT (3 mg mL^{-1} Fe conc., 2 mL) was mixed with PLL solution (0.1 mg mL^{-1}, 2 mL) in an ultrasonic bath for 3 h, causing PLL to wrap around the particle to obtain ESIO + PLL or FMT + PLL. Next, ESIO, FMT, ESIO + PLL and FMT + PLL were added respectively (1 mL) to the MSC culture medium (9 mL), and then the medium was filtered by 220 nm filter membrane for subsequent use. Typically, when MSCs in the 6 well culture plate grew to 5×10^4, the former culture medium was replaced with the culture medium containing ESIO, FMT, ESIO + PLL and FMT + PLL for incubation separately. 24 h later, the MSCs were collected and fixed in paraformaldehyde (0.4%, 100 μL), the T_1 MR images were recorded and the relaxometric data were measured on a 3T MR scanner. The iron concentration labelling of the MSCs was then quantified by ICP-MS after cell nitrolysis.

ESIO MRI test in brain and abdominal tissue of rats

Firstly, the rats were anaesthetized intraperitoneally by using chloral hydrate (10%, 3 mL kg^{-1}) then fixed in brain stereotaxic apparatus. The sample (each 0.2 mg Fe per kg, 15 μL) was injected into the corpus striatum region for 20 min. 8 h later, the rats were anaesthetized and fixed into a radio frequency rat head coil, and T_1 MR images were recorded on a 7T MRI small animal system scanner. On the other hand, chloral hydrate (10%, 3 mL kg^{-1}) was intraperitoneally injected for anaesthesia, then the ESIO solution (3 mg Fe per kg) was administrated to the rat subcutaneous abdomen tissue. 30 min later, the T_1 MR images were recorded on a 7T MRI scanner with a rat body coil.

Statistical analysis

Differences of group *versus* control were determined by applying Student's *t*-test or by a one-way ANOVA followed by the Student–Newman–Keuls test using Sigma Stat version 3.5. The significance level was fixed as $*P < 0.05$, $**P < 0.01$, $n = 3$.

Conflicts of interest

There are no conflicts of interest to declare.

Acknowledgements

The research is supported by the grant received from the National Key Research and Development Program of China (2017YFA0104302), National Natural Science Innovative Research Group Project (61821002), Natural Science Foundation of Jiangsu province (BK20190938), Key Projects of the National Natural Science Foundation of China (51832001) and National Natural Science International Cooperation Project (61420106012). We are thankful for the enormous assistance in the animal tests by Prof. Honghong Yao from Southeast University and Dr Xiaoli Mai from Drum Tower Hospital in Nanjing.

1 Z. Qin, Y. Li and N. Gu, *Adv. Healthcare Mater.,* 2018, **7,** 1800347.

2 Y. Liu, M. Li, F. Yang and N. Gu, *Sci. China Mater.,* 2017, **60,** 471–486.

3 K. Zhu, Y. Ju, J. Xu, Z. Yang, S. Gao and Y. Hou, *Acc. Chem. Res.,* 2018, **51,** 404–413.

4 S. E. Kim, L. Zhang, K. Ma, M. Riegman, F. Chen, I. Ingold, M. Conrad, M. Z. Turker, M. H. Gao, X. J. Jiang, S. Monette, M. Pauliah, M. Gonen, P. Zanzonico, T. Quinn, U. Wiesner, M. S. Bradbury and M. Overholtzer, *Nat. Nanotechnol.,* 2016, **11,** 977–985.

5 S. Zanganeh, G. Hutter, R. Spitler, O. Lenkov, M. Mahmoudi, A. Shaw, J. S. Pajarinen, H. Nejadnik, S. Goodman, M. Moseley, L. M. Coussens and H. E. Daldrup-Link, *Nat. Nanotechnol.,* 2016, **11,** 986–994.

6 Q. Wang, B. Chen, M. Cao, J. Sun, H. Wu, P. Zhao, J. Xing, Y. Yang, X. Zhang, M. Ji and N. Gu, *Biomaterials,* 2016, **86,** 11–20.

7 Q. Wang, B. Chen, F. Ma, S. Lin, M. Cao, Y. Li and N. Gu, *Nano Res.,* 2017, **10,** 626–642.

8 H. Chen, J. Sun, Z. Wang, Y. Zhou, Z. Lou, B. Chen, P. Wang, Z. Guo, H. Tang, J. Ma, Y. Xia, N. Gu and F. Zhang, *ACS Appl. Mater. Interfaces,* 2018, **10,** 44279–44289.

9 A. C. Vandergriff, T. M. Hensley, E. T. Henry, D. L. Shen, S. Anthony, J. Y. Zhang and K. Cheng, *Biomaterials,* 2014, **35,** 8528–8539.

10 J. J. Lamanna, J. Gutierrez, L. N. Urquia, C. V. Hurtig, E. Amador, N. Grin, C. N. Svendsen, T. Federici, J. N. Oshinski and N. M. Boulis, *Stem Cells Transl. Med.,* 2017, **6,** 139–150.

11 P. Wang, N. Gu, J. Sun, S. Ma, G. Ning, W. Chen, B. Wang, D. Ye, B. Chen, Y. Yang and Q. Jiang, *IEEE Trans. Biomed. Eng.,* 2019, 10.1109/tbme.2019.2931774.

12 B. H. Kim, N. Lee, H. Kim, K. An, Y. I. Park, Y. Choi, K. Shin, Y. Lee, S. G. Kwon, H. B. Na, J. G. Park, T. Y. Ahn, Y. W. Kim, W. K. Moon, S. H. Choi and T. Hyeon, *J. Am. Chem. Soc.,* 2011, **133,** 12624–12631.

13 H. Wei, O. T. Bruns, M. G. Kaul, E. C. Hansen, M. Barch, A. Wisniowska, O. Chen, Y. Chen, N. Li, S. Okada, J. M. Cordero, M. Heine, C. T. Farrar, D. M. Montana, G. Adam, H. Ittrich, A. Jasanoff, P. Nielsen and M. G. Bawendi, *Proc. Natl. Acad. Sci. U. S. A.,* 2017, **114,** 2325–2330.

14 Z. Y. Shen, T. X. Chen, X. H. Ma, W. Z. Ren, Z. J. Zhou, G. Z. Zhu, A. Zhang, Y. J. Liu, J. B. Song, Z. H. Li, H. M. Ruan, W. P. Fan, L. S. Lin, J. Munasinghe, X. Y. Chen and A. G. Wu, *ACS Nano,* 2017, **11,** 10992–11004.

15 J. X. Lu, J. H. Sun, F. Y. Li, J. Wang, J. N. Liu, D. Kim, C. H. Fan, T. Hyeon and D. S. Ling, *J. Am. Chem. Soc.,* 2018, **140,** 10071–10074.

16 A. J. Theruvath, H. Nejadnik, A. M. Muehe, F. Gassert, N. J. Lacayo, S. B. Goodman and H. E. Daldrup-Link, *Clin. Cancer Res.,* 2018, **24,** 6223–6229.

17 D. Ling, N. Lee and T. Hyeon, *Acc. Chem. Res.,* 2015, **48,** 1276–1285.

18 H. Zhang, L. Li, X. L. Liu, J. Jiao, C. T. Ng, J. B. Yi, Y. E. Luo, B. H. Bay, L. Y. Zhao, M. L. Peng, N. Gu and H. M. Fan, *ACS Nano,* 2017, **11,** 3614–3631.

19 H. Sun, B. Zhang, X. X. Jiang, H. L. Liu, S. M. Deng, Z. Li and H. B. Shi, *Nanomedicine,* 2019, **14,** 5–17.

20 E.-A. Park, W. Lee, Y. H. So, Y.-S. Lee, B.-s. Jeon, K. S. Choi, E.-g. Kim and W.-J. Myeong, *Invest. Radiol.,* 2017, **52,** 128–133.

21 Z. Y. Jia, L. N. Song, F. C. Zang, J. C. Song, W. Zhang, C. Z. Yan, J. Xie, Z. L. Ma, M. Ma, G. J. Teng, N. Gu and Y. Zhang, *Theranostics,* 2016, **6,** 1780–1791.

22 B. Chen and N. Gu, *Mater. China,* 2017, **36,** 211–218.

23 B. Chen, J. Sun, Y. Han and N. Gu, *Sci. Sin.: Chim.,* 2019, 10.1360/SSC-2019-0019.

24 A. P. LaGrow, M. O. Besenhard, A. Hodzic, A. Sergides, L. K. Bogart, A. Gavriilidis and T. Nguyen Thi Kim, *Nanoscale,* 2019, **11,** 6620–6628.

25 B. Chen, Y. Li, X. Zhang, F. Liu, Y. Liu, M. Ji, F. Xiong and N. Gu, *Mater. Lett.,* 2016, **170,** 93–96.

26 Y. Li, K. Hu, B. Chen, Y. Liang, F. Fan, J. Sun, Y. Zhang and N. Gu, *Colloids Surf., A,* 2017, **520,** 348–354.

27 F. Fan, J. Sun, B. Chen, Y. Li, K. Hu, P. Wang, M. Ma and N. Gu, *Sci. China Mater.,* 2018, **61,** 1112–1122.

28 B. Chen, J. Sun, F. Fan, X. Zhang, Z. Qin, P. Wang, Y. Li, X. Zhang, F. Liu, Y. Liu, M. Ji and N. Gu, *Nanoscale,* 2018, **10,** 7369–7376.

29 Y. Cao, W. Geng, R. Shi, L. Shang, G. I. N. Waterhouse, L. Liu, L.-Z. Wu, C.-H. Tung, Y. Yin and T. Zhang, *Angew. Chem., Int. Ed.,* 2016, **55,** 14952–14957.

30 S. L. Cumberland, K. M. Hanif, A. Javier, G. A. Khitrov, G. F. Strouse, S. M. Woessner and C. S. Yun, *Chem. Mater.,* 2002, **14,** 1576–1584.

31 T. G. Lei, J. N. Calata, G. Q. Lu, X. Chen and S. F. Luo, *IEEE Trans. Compon., Packag. Technol.,* 2010, **33,** 98–104.

32 J. Garside, *Chem. Eng. Sci.,* 1985, **40,** 3–26.

33 J. Zhang, H. Li, Q. Kuang and Z. Xie, *Acc. Chem. Res.,* 2018, **51,** 2880–2887.

34 D. L. Ni, J. W. Zhang, J. Wang, P. Hu, Y. Y. Jin, Z. M. Tang, Z. W. Yao, W. B. Bu and J. L. Shi, *ACS Nano,* 2017, **11,** 4256–4264.

35 E. J. Werner, A. Datta, C. J. Jocher and K. N. Raymond, *Angew. Chem., Int. Ed.,* 2008, **47,** 8568–8580.

36 S. H. Lee, B. H. Kim, H. B. Na and T. Hyeon, *Wiley Interdiscip. Rev.: Nanomed. Nanobiotechnol.,* 2014, **6,** 196–209.

37 Z. Lou, C. Yuan, Y. Zhang, Y. Li, J. Cai, L. Yang, W. Wang, H. Han and J. Zou, *J. Alloys Compd.,* 2019, **775,** 800–809.

38 M. A. Boles, D. Ling, T. Hyeon and D. V. Talapin, *Nat. Mater.,* 2016, **15,** 141–153.

39 Z. Lou, R. Li, P. Wang, Y. Zhang, B. Chen, C. Huang, C. Wang, H. Han and Y. Li, *Chem. Eng. J.,* 2019, 123571, 10.1016/j.cej.2019.123571.

40 J. S. Choi, S. Kim, D. Yoo, T. H. Shin, H. Kim, M. D. Gomes, S. H. Kim, A. Pines and J. Cheon, *Nat. Mater.,* 2017, **16,** 537; –+

41 X. Y. Zheng, K. Zhao, J. Tang, X. Y. Wang, L. D. Li, N. X. Chen, Y. J. Wang, S. Shi, X. Zhang, S. Malaisamy, L. D. Sun, X. Wang, C. Chen and C. H. Yan, *ACS Nano,* 2017, **11,** 3642–3650.

42 H. Y. Xing, S. J. Zhang, W. B. Bu, X. P. Zheng, L. J. Wang, Q. F. Xiao, D. L. Ni, J. M. Zhang, L. P. Zhou, W. J. Peng, K. L. Zhao, Y. Q. Hua and J. L. Shi, *Adv. Mater.,* 2014, **26,** 3867–3872.

43 Z. Lou, R. Li, P. Wang, Y. Zhang, B. Chen, C. Huang, C. Wang, H. Han and Y. Li, *Chem. Eng. J.,* 2019, 123571, 10.1016/j.cej.2019.123571.

44 D. Ye, Y. Li and N. Gu, *Nano Res.,* 2018, **11,** 2970–2991.

45 D. Ye, Q. Wang, W. Zhang, J. Sun and N. Gu, *Chin. Sci. Bull.,* 2017, **62,** 2301–2311.

46 V. Ayala, A. P. Herrera, M. Latorre-Esteves, M. Torres-Lugo and C. Rinaldi, *J. Nanopart. Res.,* 2013, **15,** 1874–1887.

47 F. Q. Hu, Q. J. Jia, Y. L. Li and M. Y. Gao, *Nanotechnology,* 2011, **22,** .

48 L. H. Shen, J. F. Bao, D. Wang, Y. X. Wang, Z. W. Chen, L. Ren, X. Zhou, X. B. Ke, M. Chen and A. Q. Yang, *Nanoscale,* 2013, **5,** 2133–2141.

49 G. M. Huang, R. Liu, Y. H. Hu, S. H. Li, Y. Wu, Y. Qiu, J. Y. Li and H. H. Yang, *Sci. China: Chem.,* 2018, **61,** 806–811.

50 T. Borase, T. Ninjbadgar, A. Kapetanakis, S. Roche, R. O'Connor, C. Kerskens, A. Heise and D. F. Brougham, *Angew. Chem., Int. Ed.,* 2013, **52,** 3164–3167.

51 K. Y. Ju, J. W. Lee, G. H. Im, S. Lee, J. Pyo, S. B. Park, J. H. Lee and J. K. Lee, *Biomacromolecules,* 2013, **14,** 3491–3497.

52 L. Sandiford, A. Phinikaridou, A. Protti, L. K. Meszaros, X. J. Cui, Y. Yan, G. Frodsham, P. A. Williamson, N. Gaddum, R. M. Botnar, P. J. Blower, M. A. Green and R. T. M. de Rosales, *ACS Nano,* 2013, **7,** 500–512.

Queries and Answers

Query: Funder details have been incorporated in the funder table using information provided in the article text. Please check that the funder information in the table is correct.
Answer: The funder information in the table is totally correct. “The National Natural Science International Cooperation Project (61420106012)” in the Acknowledgements text should be removed.

Query: For your information: You can cite this article before you receive notification of the page numbers by using the following format: (authors), Nanoscale, (year), DOI: 10.1039/c9nr10397j.
Answer: Thank you for the information.

Query: Please confirm that the spelling and format of all author names is correct. Names will be indexed and cited as shown on the proof, so these must be correct. No late corrections can be made.
Answer: “Zang Fengchao” should be changed with “Fengchao Zang”. The First name is “**Fengchao**”, and the last name is “**Zang**”.

Query: The sentence beginning “Then, the solution …” has been altered for clarity, please check the meaning has not changed.
Answer: The alternation is fine.

Query: AU: The sentence beginning “The time at each…” has been altered for clarity, please check the meaning has not changed.
Answer: The alternation is fine.

Query: In the sentence beginning “Additionally, in order …”, the phrase “attached material” is unclear, please provide an alternative phrase.
Answer: The “attached material” can be replaced with “**coating material**”.

Query: The word “alleviate” in the sentence beginning “In our experiment, …” is unclear, please provide an alternative word.
Answer: The “alleviate” can be replaced with “**affect**”.

Query: The sentence beginning “ESIO-1 forms …” has been altered for clarity, please check the meaning has not changed.
Answer: The alternation is fine.

Query: The sentence beginning “Given the neutral …” has been altered for clarity, please check the meaning has not changed.
Answer: The alternation is fine.

Query: “signal” appears to be spelled incorrectly as “sinal” in Fig. 4b. Please could you supply a corrected version (preferably as a TIF file at 600 dots per inch) with your proof corrections.
Answer: Please check the new figure attached.

Query: The sentence beginning “The iron oxide …” has been altered for clarity, please check the meaning has not changed.
Answer: The alternation is fine.

Query: In the sentence beginning “PSC (the coating …”, should “pharmaceutical items” be changed to “pharmaceutical properties”?
Answer: The “pharmaceutical item” can be replaced with “pharmaceutical properties”.

Query: Ref. 11 and 23: Can these references be updated? If so, please provide the relevant information such as year, volume and page or article numbers as appropriate.
Answer: The reference 23 can be cited as “B. Chen, J. Sun, Y. Han and N. Gu, *Sci. Sin: Chim.*, 2019, **49**, 1156-1167”. The reference 11 has not been updated.

Query: Ref. 24: Please check that the name for the 7h author is displayed correctly.
Answer: The 7th author should be cited as “**N. T. K. Thanh**”.

Query: Ref. 40: Please provide details of the last page number for this article.
Answer: The page number of reference 40 is “537-**542**”.

Query: Ref. 47: Please provide the page (or article) number(s).
Answer: The article number of reference 47 is “**245604**”.